INSTITUTO SUPERIOR TÉCNICO

UNIVERSIDADE DE LISBOA

*1º Semester 2023/2024*

# Computational Fluid Mechanics

---

## 4th Computational Exercise: Compressible Viscous and Inviscid High Speed Flows

---

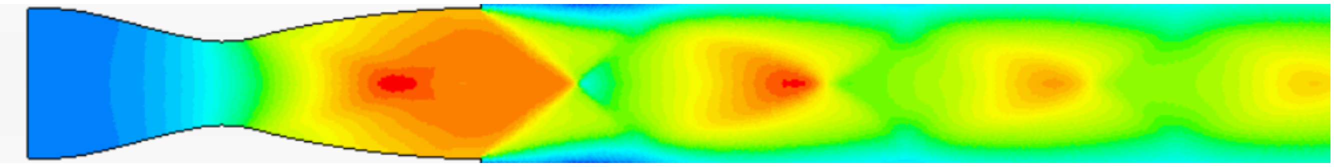

**GROUP NUMBER 7**
João Fernandes Marques, 93270
Miguel Dias Casalinho, 93307
João Pedro Sousa Gaspar, 96930
Pedro Afonso Simões Gonçalves, 105745

**February 13, 2025**

# Contents

# 1 Introduction

In the realm of fluid dynamics, Computational Fluid Dynamics (CFD) has emerged as a powerful tool for simulating and analyzing complex fluid flow phenomena. This project delves into two critical aspects of CFD – the simulation of a convergent-divergent nozzle and a shock tube, each presenting unique challenges and insights into fluid behaviour.

The first segment of this study focuses on the simulation of a convergent-divergent nozzle, a fundamental component in aerospace engineering and propulsion systems. The objective is to employ CFD techniques to model the flow through an axisymmetric nozzle and subsequently compare the results with theoretical expectations. For this, both inviscid and viscous flow simulations were conducted to explore the impact of viscosity on the nozzle's performance.

The second phase of our project involves the simulation of a shock tube, a crucial device in fluid dynamics experiments and the study of compressible flows. Here, the primary goal is to utilize CFD methodologies to reproduce the shock wave and general flow behaviour within the tube and subsequently compare the simulated outcomes with theoretical predictions.

# 2 Convergent-Divergent Nozzle

The first segment of this comprehensive study focuses on the simulation of convergent-divergent nozzles using CFD. Convergent-divergent nozzles play a pivotal role in aerospace engineering and propulsion systems, influencing the efficiency and performance of various applications. In this phase, the goal is to apply viscous and inviscid simulations with STAR CCM+ and compare the results with 1D isentropic/plane shock theory in two distinct scenerios: complete isentropic flow through the noozle and a case where a shock is present inside it. An overview of the mesh and numerical parameters utilize in the simulations are also presented, as well as other flow phenomena that could be observed with this simulation setups and that the group decided it was worth mentioning.

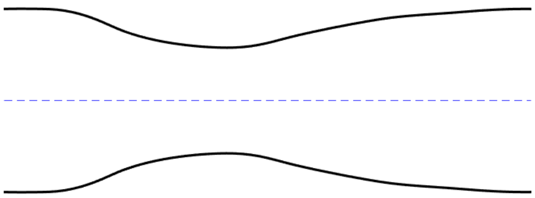

Figure 1: Nozzle Geometry

## 2.1 Domain and Boundary conditions

In order to correctly solve this problem, special care had to be taken with the geometry of the domain, since it plays a important role on the results. The group decided to utilise the same general geometry presented in the problem statement with only a radial section of the nozzle being modelled. The model needed to be the same for both inviscid and viscous simulations so to fairly compare the results in each. This lead to constraints in its geometry, specially due to the viscous simulations, where flow separation is a problem that should be addressed. This is not a problem for the full isentropic case because the flow constantly encounters favourable pressure gradients. This is not true when there is a shock wave.

If a shock wave is present at the diverging part of the nozzle, the flow turns to subsonic at a point where the nozzle is increasing its cross sectional area. This causes the flow to decelerate, because it is subjected to a highly adverse pressure gradient, in contrast to the supersonic flow that reduces pressure as cross sectional area increases. The phenomena indicates that the longer the nozzle, the lower needs to be the gradient of cross-sectional area of the nozzle, resulting in the mitigation of this phenomena. While this is mainly used in supersonic wind tunnels, this brings practical problems in real applications where weight limitations are an important design factor, namely, propulsion systems. So, for this work an intermediate approach was selected, where the nozzle size was chosen to limit separation but without excessively extending the diverging section. In addition to the nozzle, a atmospheric chamber is added at its exit to allow full flow development after leaving the nozzle.

Regarding boundary conditions, a total pressure was defined in the inlet, as well as an initial total temperature. While the total temperature remained constant through all 4 simulations, the total pressure needed to be changed so that the shocks could be created and moved in the domain. For the selection of this value, results from quasi 1D flows needed to be computed. A code was created to perform the necessary calculations and the values required for the isentropic case and for the shock in a specific location were calculated. The initial total pressure was then used in the STAR CCM+ calculations. For the outlet, a pressure outlet at atmospheric condition was chosen to allow full expansion of the flow after the nozzle exit. An axisymmetric condition was set in the axis of rotation and the other boundaries were set as no-slip walls.

The mesh chosen to perform the computations is a polyhedral grid which showed the best convergence behaviour from quadrilateral and triangular. To correctly discretize the boundary layer, $y+ < 5$ an inflation layer was added which included a total thickness of X and Y elements. The final mesh for each condition is presented in Figure 2. As can be seen, 3 distinct refinement zones were added with the finest region of the viscous mesh slightly decrease in order to facilitate convergence and reduce computational time.

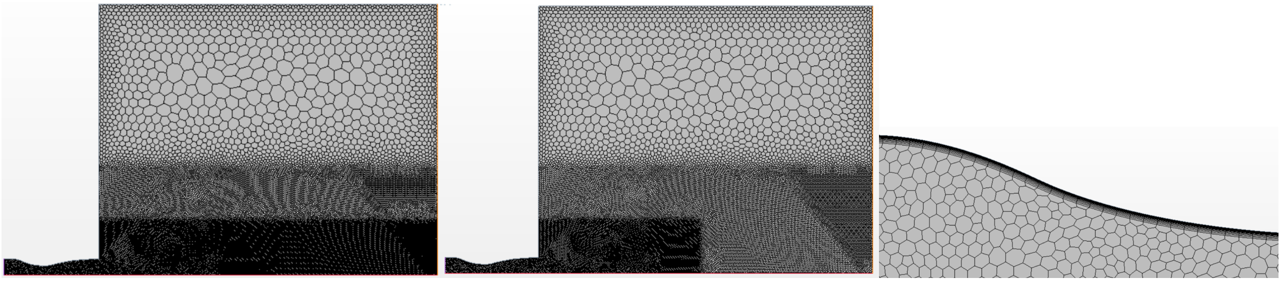

(a) Inviscid Grid

(b) Viscous Grid

(c) Inflation layer detail

Figure 2: Mesh topology utilised

## 2.2 Models and Convergence

As mentioned in the introductory text, two types of flow are to be modeled, namely viscous flow and inviscid flow. In both types, the flow is considered in steady conditions and axisymmetric with the air behaving as an ideal gas. In both cases compressible flow is solved. While for the inviscid case no more models where needed, the viscous case required a turbulence model for the completion of the RANS equations. The turbulence model chosen was the k-w SST model since it has been shown to give accurate results in this type of applications [1].

Convergence criteria was set to $10^{-7}$ for all cases. In order to ensure convergence relaxation values needed to be fine tuned to each simulation.

## 2.3 Results and discussion

In this section, the results from the simulations are analysed and then compared with the Quasi One Dimensional case. For the theoretical cases, a MATLAB code was made for easy representation and comparison between cases (see Appendix 5.1). The nozzle dimensions were exported from the STAR CCM simulations and used as an input to compute the theoretical values using isentropic and normal shock relations (equations 1 and 2, respectively). In this equations, $A^*$ represents the critical throat area, $M_x$ mach number just before the shock and $M_y$ mach number just after the shock.

$$\left(\frac{A}{A^*}\right)^2 = \frac{1}{M^2}\left[\frac{2}{\gamma+1}\left(1+\frac{\gamma-1}{2}M^2\right)\right]^{(\gamma+1)/(\gamma-1)} \tag{1}$$

$$M_y^2 = \frac{1+[(\gamma-1)/2]M_x^2}{\gamma M_x^2-(\gamma-1)/2} \tag{2}$$

From the analytical results of $M$, the pressure can be computed in the entire nozzle using equation 3, considering that at the outlet of the nozzle, the pressure is know and is $p_{atm} = 101325Pa$. For the isentropic case of section 2.3.1, the stagnation pressure $p_0$ is constant through the entire flow, and thus can be directly calculated at the outlet of the nozzle. In this case, the stagnation pressure obtained to ensure isentropic conditions was $p_0$ above $2142750Pa$. In the shock case of section 2.3.2, the stagnation pressure was calculated before and after the shock, since through the shock wave there's energy dissipation that needed to be considered in order to obtain accurate results. From this analysis the shock case was conducted with a inlet total pressure of $173790Pa$.The entire code that was used is displayed in the appendix 5.1, and the results of the case with shock wave were validated using example 5.6 of [2].

$$\frac{p_o}{p} = \left(1 + \frac{\gamma - 1}{2} M^2\right)^{\gamma/(\gamma-1)} \tag{3}$$

This comparison is not meant as a validation process since the models used are not the same: while the axisymmetric model is being solved by STAR CCM+, the theoretical results are relative to a Quasi One Dimensional model. The area relations were adapted for the latter case by squaring the $y$ coordinate of the geometry used in the CFD simulation. The STAR CCM+ data of Mach and pressure displayed in the plots of this report was taken from the centerline of the nozzle.

### 2.3.1 Isentropic Case

The results of Mach and pressure for the isentropic cases are plotted in Figures 3 and 4, respectively. Visual results can also be seen in Figures 5 and 6 .At the converging section, the mach and pressure results are essentially the same for all 3 models, the flow enters subsonic and at the throat Mach number is sonic. But after that, while the two CFD models stay in agreement, the Quasi 1D model shows a different behaviour especially at the end of diverging portion. The pressure at the outlet is practically the same for all of the models (and consequently Mach too) but the inviscid model shows a slightly smaller pressure at the outlet. This can be explained by the theory behind the Fanno Flow, where the presence of friction forces causes supersonic flow to decelerate, in addition, the formation of the boundary layer in the viscous simulation acts as a constrain to the flow, reducing effective area, which for supersonic flow, also leads to its deceleration as seen in 3.

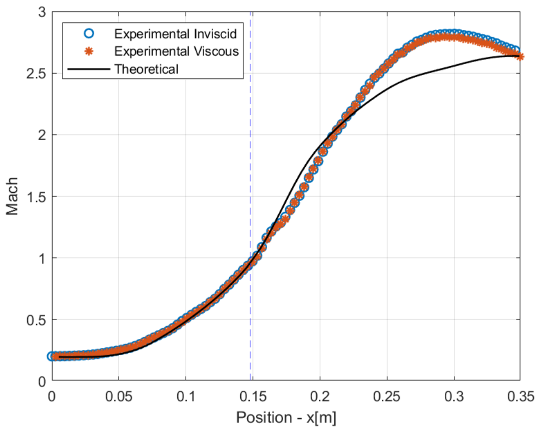

Figure 3: Mach variation for isentropic case

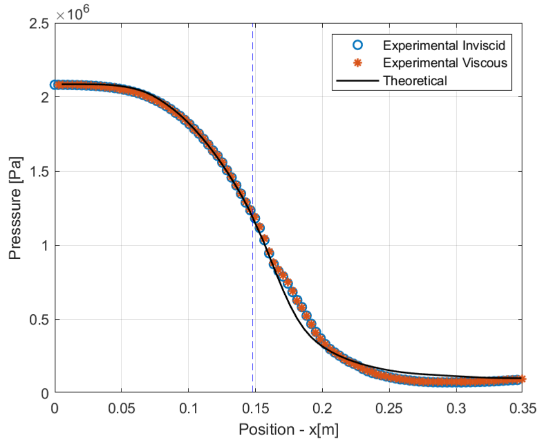

Figure 4: Pressure variation for isentropic case

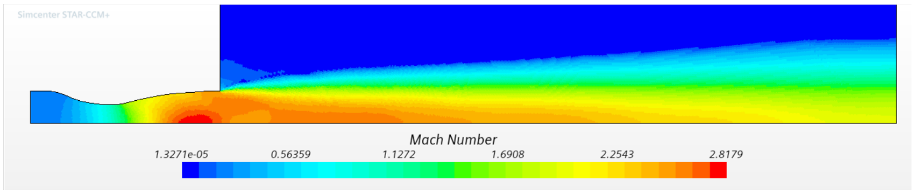

Figure 5: mach inv

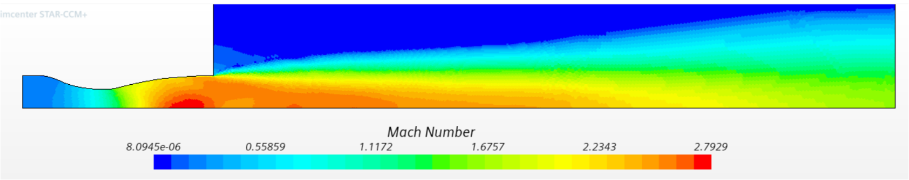

Figure 6: mach visc

The presence of the boundary layer changes the overall shape of the nozzle in terms of effective cross sectional area, leading to differences in flow properties also changes other parameters such as the relation between the exit area and the critical area. This by itself makes the solving problem much more complex. The presence of the no-slip condition can be verified with a visual comparison between Figures 7 and 8, where in the latter, the Mach (velocity) can be seen going to zero.

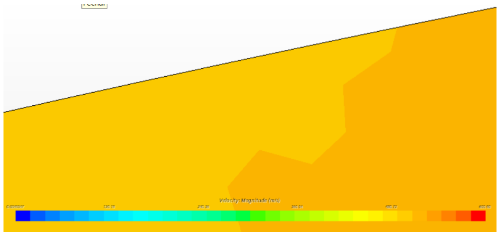

Figure 7: Wall detail (Inviscid)

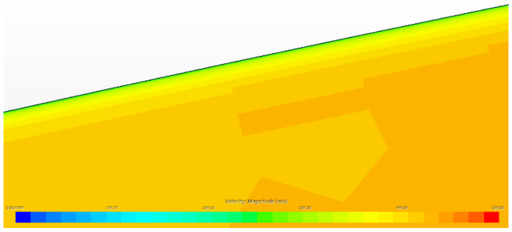

Figure 8: Wall detail (Viscous)

### 2.3.2 Shock Case

The results of Mach and pressure for the shock wave cases are plotted in Figures 9 and 10, respectively. As it was seen before for the isentropic case, at the converging portion of the nozzle, the 3 models show reasonable accordance. After the throat, but before the shock, both CFD simulations have the same Mach (analytical model has higher Mach), but pressure is smaller for the inviscid one. The shock wave happens sooner for the viscous model, the inviscid model's shock is next and finally for the analytical model that uses the normal shock model (equation 2), the shock takes place the latest. The different behaviour between the models can also be justified by the presence of the boundary layer, similar to what happened with the isentropic case. Effective cross sectional area is decreased which makes the shock happen sooner for viscous flow. To note the different behaviour of the flow after the shock, decelerating with area increases, typical to subsonic flow.

As explained in the introductory sections, after the shock, flow separation is very likely, due to the nozzle area increasing and the flow being subsonic, which causes an adverse pressure gradient. The presence of this separation in the simulation performed 14 may be the main origin for the oscillations in Mach and pressure values found just after the shock.

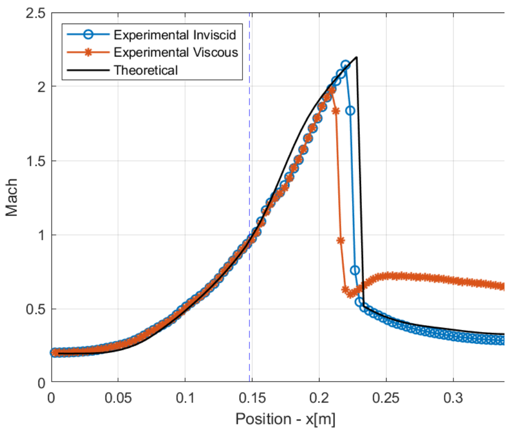

Figure 9: Mach variation for shock case

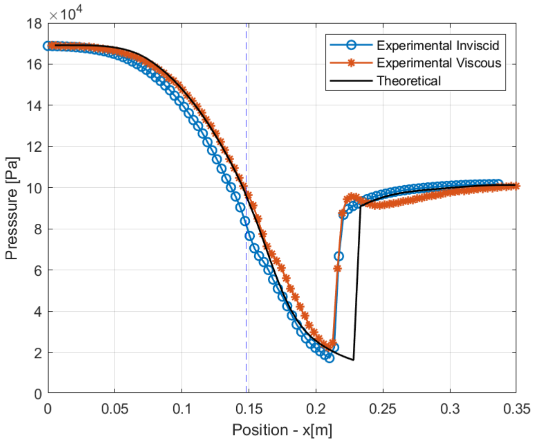

Figure 10: Pressure variation for shock case

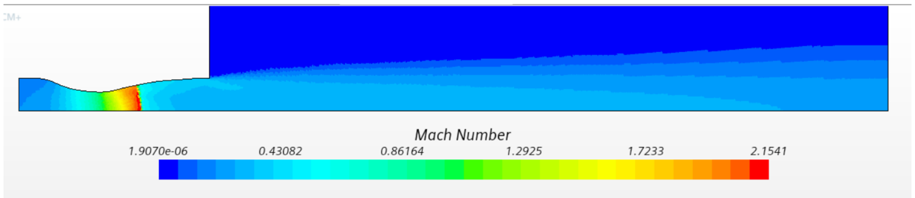

Figure 11: mach inv shock

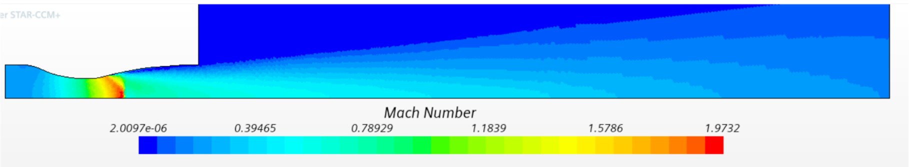

Figure 12: mach visc shock

The presence of shocks inside the nozzle causes loss in its efficiency and are not desired for the vast majority of its applications. This loss in efficiency can be represented by the total pressure of the flow (13). As is presented, the total pressure suffers an abrupt reduction through the shock wave, with the total pressure difference being higher for the inviscid flow. The loss of total pressure is a result of the conversion of kinetic energy into internal energy inside the shock. In viscous flow, viscosity allows for the dissipation of kinetic energy in the form of heat along the shock wave resulting in a lower total pressure loss across the shock.

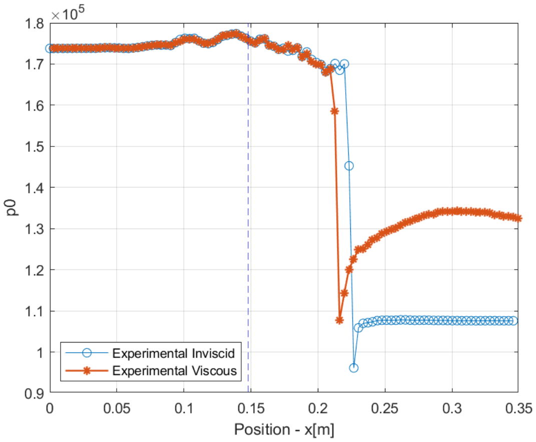

Figure 13: Total pressure variation for shock case

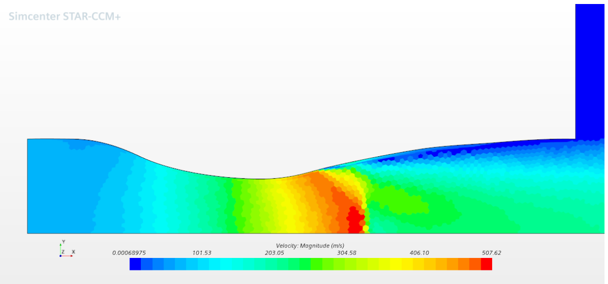

Figure 14: Detail of flow separation after shock

### 2.3.3 Other flow scenarios

In addition to the main flows intended to be analysed with this problem, this subsection shows other flow patterns possible with a converging-diverging geometry, just by varying inlet total pressure. All simulations utilize inviscid flow. If pressure is very close to the atmospheric pressure, critical flow is not reached in the throat, with subsonic regime in all domain (Fig. 15) namely full subsonic conditions throughout the nozzle. As pressure in the reservoir increases, sonic conditions are reached, with a shock forming inside the nozzle (shock condition analysed in the main work).

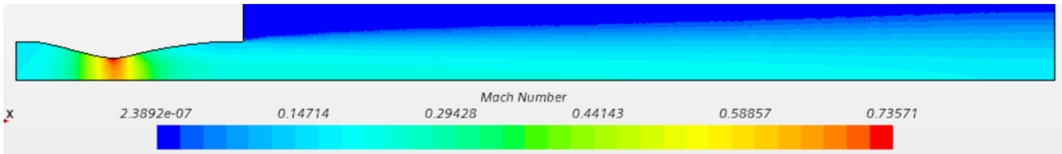

Figure 15: Mach for a Subsonic nozzle

At a certain total pressure, the shock passes the exit of the nozzle, forming a oblique shock at the exit (overexpanded nozzle) (Fig. 16). A pressure is reach such that flow is isentropic throughout(isentropic condition analysed in the main work). If pressure keeps increasing, underexpantion condition is reached, with an expansion wave at the noozle exit (Fig. 17).

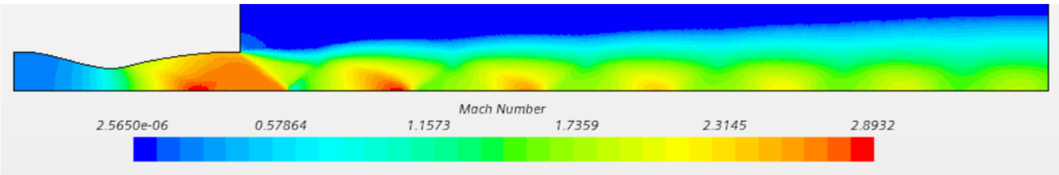

Figure 16: Mach for a Overexpended nozzle

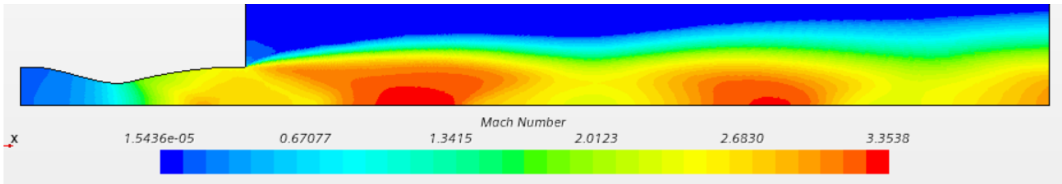

Figure 17: Mach for a Underexpended nozzle

## 3 1D Sod's Shock Tube

The shock tube is a crucial tool in fluid dynamics research, facilitating not only the study of compressible flows and shock wave interactions but also combustion reactions. In this section, the second problem of this project is addressed in which the Sod's Shock Tube is solved through the use of CFD and then compared with the analytical results. This problem is a benchmark test commonly used for code verification purposes.

The Sod shock tube is a simple but powerful tool for studying shock waves and rarefaction waves in a gas. The problem consists of a tube filled with two different gases, one high-density and high-pressure and the other low-density and low-pressure. When the diaphragm separating the two gases is suddenly removed, the gases mix and form a shock wave and a rarefaction wave. The shock wave propagates through the gas, compressing and heating it, while the rarefaction wave propagates in the opposite direction, expanding and cooling the gas. The behaviour of these waves can be used to understand a wide range of phenomena, including explosions, collisions, and the structure of the atmosphere.

### 3.1 Theoretical models

Sod's shock tube represents a unique instance within the broader framework of Riemann problems. The Riemann problem, a conceptual construct in mathematics, serves as a model to elucidate the dynamics of a gas confronted with the sudden juxtaposition of two distinct states (e.g., varying densities, pressures and velocities), resulting in a pronounced discontinuity. This phenomenon is aptly described by the Euler equations, a collection of hyperbolic partial differential equations grounded in the principles of mass, momentum, and energy conservation.

The formulation of the Riemann problem adopts the guise of an initial value problem, where the initial conditions manifest as the disparate states of the gas on either side of the disruptive juncture. The primary objective is to ascertain the solution to the governing equations of gas dynamics (Euler equations) that encapsulate its evolution over time subsequent to the emergence of the discontinuity. The derived solution manifests as a series of waves propagating trough the gas, encompassing diverse types such as shock waves, rarefaction waves, and contact discontinuities. While analytical solutions exist for certain rudimentary scenarios, the majority of practical applications necessitate the employment of numerical methods. In this report the results obtained with numerical models were compared with the analytical results of Hirsch [3].

## 3.2 Shock tube problem

To streamline the problem and facilitate mathematical analysis, several assumptions are incorporated. The flow is confined to one dimension (1D), the gas is idealised as perfect gas, the fluid is considered inviscid and the tube is assumed to be infinitely long.

Distinct properties characterise the two gases separated by the diaphragm, denoted as $L$ for left and $R$ for right. These properties are presented in the table 1, include a pressure ratio of 10.

| | **Density** $\rho(kg/m^3)$ | **Pressure** $p(kPa)$ | **Temperature** $T(K)$ | **Velocity** $v(m/s)$ |
|---|---|---|---|---|
| **Left Gas Side** | 1 | $1\times10^5$ | 348.43 | 0 |
| **Right Gas Side** | 0.01 | $1\times10^3$ | 348.43 | 0 |

Table 1: Properties of the two gases.

Upon the instantaneous removal of the diaphragm, a shock wave gives rise to five distinct zones withing the tube, as depicted in figure .The corresponding x-values are specific to the case under examination, considering the mention properties, and the time instant $t = 0.0039s$.

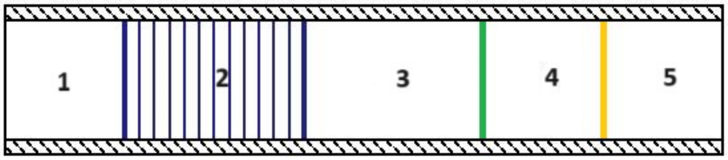

Figure 18: Shock Tube Representation

Zone 1 and 5 illustrate the initial conditions on either side of the tube. When the diaphragm ruptures at time $t = 0$, a pressure discrepancy travels to the right within the low-pressure gas, concomitantly triggering an expansion fan that propagates leftward in the high-pressure gas. Simultaneously, a contact discontinuity, demarcating the two gas zone, moves to the right within the tube.

Zone 2, represented by the striped region, exemplifies the expansion wave, where flow properties undergo continuous variations, as elaborated upon later. The green line delineating regions 3 and 4 signifies the contact discontinuity. Within these regions, pressure and velocity remain constant, while density, entropy, and Mach number experience a discontinuity. The shock wave is denoted by the yellow line, marking the boundary between regions 4 and 5.

## 3.3 Numerical Models

Given that this problem was initially designed to assess various numerical methods, this section will present insights into two employed techniques: ROE-FDS and AUSM+FVS. Both methods are designed to address the Euler equations previously mentioned, accommodating a broad spectrum of flow conditions ranging from subsonic to supersonic. Notably, they exhibit a capacity to handle discontinuities with high precision and stability.

The Roe Flux Differencing Scheme is a numerical methodology, rooted in Godunov's scheme, utilised for approximating solutions to partial differential equations (PDEs) governing fluid flow. It employs the Roe averaging technique, which combines the left and right states of a fluid at specific point in space and time through a linear combination to calculate the flux at that point.

AUSM+FVS (Advection Upstream Spitting Method plus Flux Vector Splitting) represents another numerical approach that divides the flux into two components: convective and pressure parts. The Flux Vector Splitting aids in capturing the influence of neighbouring fluid states effectively. Upwind differences play a crucial role in this scheme.

## 3.4 Numerical Results

To conduct the numerical simulations, it was imperative to establish certain parameters: Employed a second-order spatial discretization and implicit temporal discretization; Defined the time step for numerical solver analysis at $t = 1 \times 10^{-4}$ s; Maintained a constant Courant number at 50; Imposed a maximum of 10 inner iterations.

The repercussions of altering the time step and the maximum inner iterations on the numerical solution will be scrutinized in subsquent analysis.

### 3.4.1 Mesh Generation

Althouth the problem is one-dimensional, the mesh is constructed in a three-dimensional manner. Innitiallly, a 20-meter block is generated and partitioned into sections, with each cell representing a small block. Subsequently, the block is simplified into a line (1D), disregarding the $y$ and $z$ coordinates and introducing a plane section at the midpoint.

The mesh is designed to have approximately 50 cells, and, due to a substantial portion of the domain exhibiting the same properties, the mesh is refined in the central region while being coarser at the beginning and end. This refinement occurs between $-4$ m and 4 m, resulting in a total of 50 cells within the block. The refinement pattern is illustrated in figure 19. The finer cells measure 0.297 m, while the coarser ones have size of approximately 0.99 m. As we will explore later, the chosen number of cells proves inadequate for revealing significant variations when altering the numerical settings.

Figure 19: Mesh generated between -10 and 10 m.

### 3.4.2 Numerical Solvers

To assess the performance of both numerical solvers, two simulations were executed. Figures 21, 22, 23 and 24, illustrates the results for four properties (pressure, density, Mach number, and entropy), while figure 20 focuses on velocity - a parameter where differences between the solvers are more pronounced. The presented domain spans from $-10$ m to 10 m.

Notably, discrepancies between the solvers become apparent in discontinuities and variations of slope, situations for which these methods are specifically designed. The Roe-FDS solver demonstrates a quicker response to variations compared to AUSM+FVS. It is observed in figure 20 the oranges dots consistently lead the blue ones. This discrepancy arises from the discretization strategies employed (central and upwind). Given that the upwind scheme excludes information from the front/right cell, it possesses less upstream flow information than the central scheme. Consequently, it only acquires that information when closer to the discontinuity. Despite the faster initial reaction to the discontinuity, the disparity is swiftly compensated, and AUSM+FVS reaches the stabilised region of the curve simultaneously or even faster than Roe-FDS.

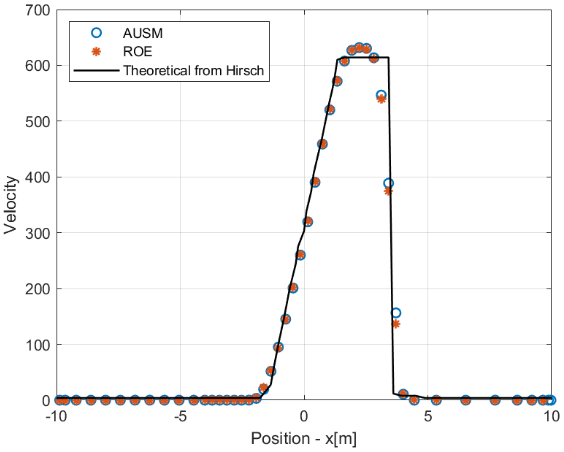

Figure 20: Comparison of the solvers analysed using velocity of air along the shock tube.

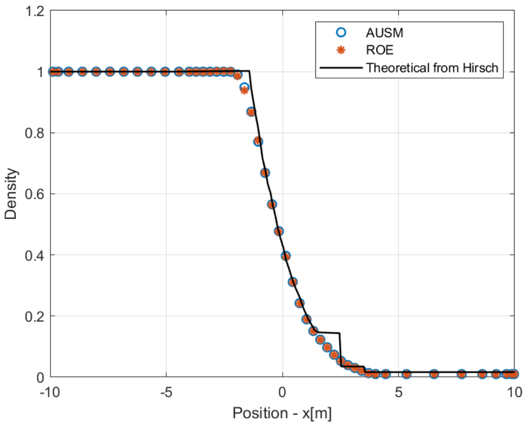

Figure 21: Comparison of the solvers analysed using density of air along the shock tube.

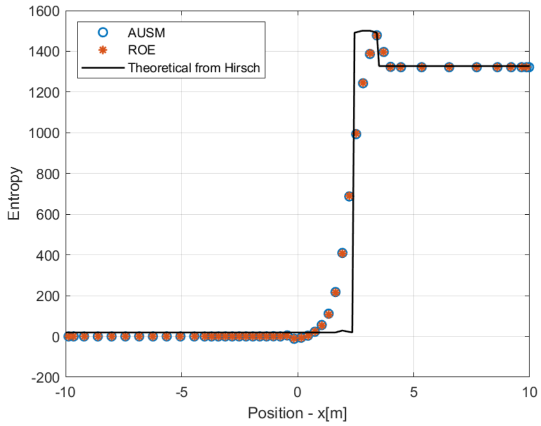

Figure 22: Comparison of the solvers analysed using Entropy of air along the shock tube.

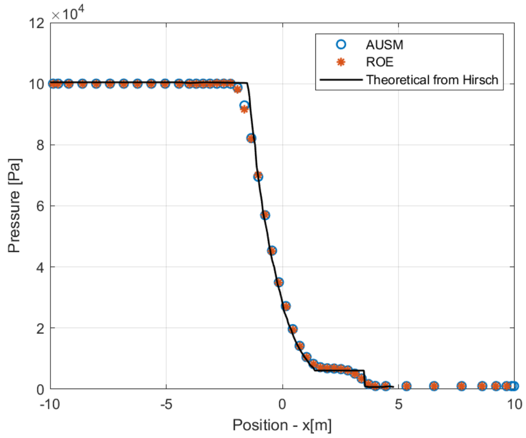

Figure 23: Comparison of the solvers analysed using pressure of air along the shock tube.

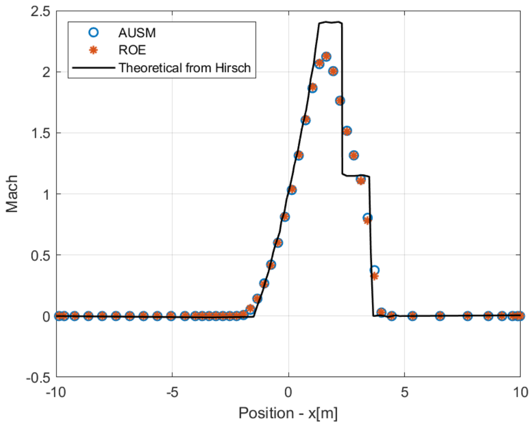

Figure 24: Comparison of the solvers analysed using Mach of air along the shock tube.

### 3.4.3 Different Times steps

In addition to exploring different solvers, various time steps were experimented with to assess their impact on the results. The chosen solver for this analysis was AUSM+FVS, with the time instant set at $t = 0.0039$ s. Three distinct time steps were selected: $t_s = 1 \times 10^{-4}$ s, $t_s = 1 \times 10^{-5}$ s and $t_s = 1 \times 10^{-6}$ s. For brevity, only the velocity will be discussed in this subsection, as it is where the variations are most pronounced.

An examination of the figure 26 unveils that significant differences only manifest in the discontinuity. In the initial slope, the circles, dots and triangles overlap, signifying no discernible variation among time steps. Notably, in the discontinuity, the larger time step exhibits an earlier response, with the triangles ($t_s = 1 \times 10^{-4}$ s) consistently leading the others.

### 3.4.4 Different maximum inner interaction

The number of inner interactions signifies the iterations executed before advancing to the subsequent time step. It serves to enhance the residuals and is expected to contribute to an improved final solution. Figure 25 illustrates the impact of this parameter on velocity.

Similar to examination of time steps, the noticeable differences across simulations, when altering the maximum number of inner iterations, are predominantly observed in the discontinuity zone. With an escalation in the number of iterations (depicted by blue circles), the numerical solution converges closer to the analytical solution, aligning with expectations.

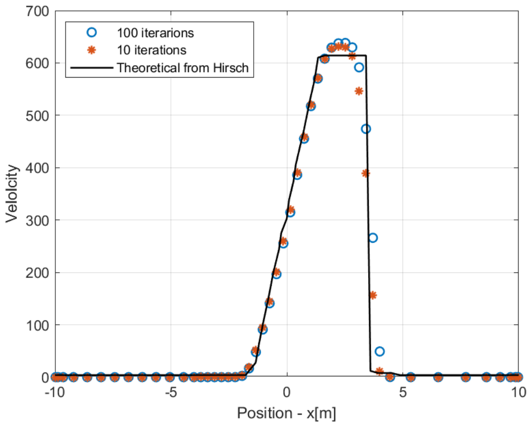

Figure 25: Comparison of the different maximum inner iterations analyzed using the velocity of air along the shock tube.

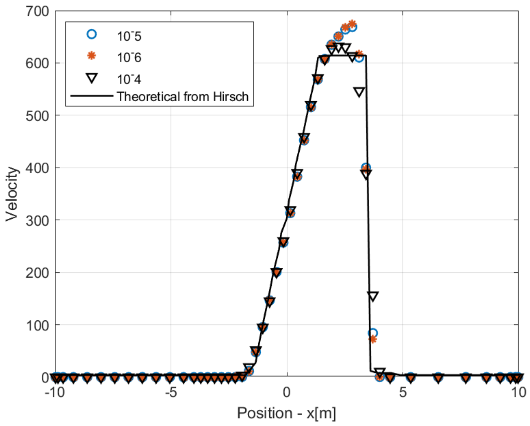

Figure 26: Comparison of the different time steps analyzed using the velocity of air along the shock tube.

# 4 Conclusion

In conclusion, our project involved two distinct simulations, each delving on the physics and applicability of compressible flow valuable insights into fluid dynamics and shock wave behavior. The results obtained through the finite volume simulations of compressible flows were compared to the analytical results obtained with classical theory.

The first part of this project focused on the CFD analysis of convergent-divergent nozzles. The results in the isentropic case without the shock for both CFD simulations are very similar and show a slight disagreement at the diverging section in comparison with the analytical results. For the case with the shock wave there's a bigger difference between models, especially in the position of the shock wave, that happens closest to the throat in the viscous model. By increasing/decreasing total pressure above the isentropic one, underexpanded/overexpanded conditions could be simulated in CFD.

The second part of this project centered around simulating a shock tube, specifically addressing Sod's problem. This classic problem serves as a benchmark for testing numerical methods in capturing shock wave interactions. The aim was to replicate the physical conditions of a shock tube and compare our results with the analytical solution. The comparison between numerical methods, specifically ROE-FDS and AUSM+FVS, revealed that AUSM+FVS produced better results that are closer to the analytical solution. Additionally, variations in time steps and inner iterations demonstrated significant impacts on the numerical solution, emphasizing the need for careful parameter selection in simulations. Overall, this study contributes insights into the capabilities and limitations of numerical methods in fluid dynamics research.

# References

[1] A. Balabel, A. Hegab, M. Nasr, and S. M. El-Behery, “Assessment of turbulence modeling for gas flow in two-dimensional convergent–divergent rocket nozzle,” *Applied Mathematical Modelling*, vol. 35, no. 7, pp. 3408–3422, 2011.

[2] J. D. Anderson, *Modern compressible flow: with historical perspective*. McGraw-Hill New York, 1990, vol. 12.

[3] C. Hirsch, *Numerical Computation of Internal and External Flows, Volume 2: Computational Methods for Inviscid and Viscous Flows*. Wiley, 1991, ISBN: 9780471924524.

# 5 Appendix

## 5.1 MATLAB code for Quasi-1D model

Listing 1: Quasi_1D_model.m

```
A_input=[3.000439189    3.002274115     2.999852088     2.989816582
    2.972326568     2.948230371     2.918469069     2.884189856     2.84672092
          2.80733904      2.768238815     2.731751497     2.697766167
    2.66456397      2.630500302     2.593937324     2.553139143     2.50595434
          2.450851713     2.387464174     2.316694279     2.241427368
    2.164070884     2.08544267      2.00572613      1.924899177     1.843444841
         1.761672129     1.679524715     1.596923484     1.513077707
    1.426252989     1.336761441     1.249396202     1.170588306     1.105236363
         1.055879148     1.022819244     1.004918243     1        1.005094242
         1.017770383     1.037090006     1.062949813     1.095532569
    1.135407193     1.182994419     1.238769308     1.304213063     1.381026186
         1.470836321     1.57597014      1.699151942     1.844613464
    2.011748972     2.187387616     2.35879452      2.520355125     2.665463739
         2.788418934     2.88558951      2.953011845     2.989460687
    3.003691701     3.0098538       3.013739676     3.014145587     3.009222487
         3.002208145
];
x_input=[-0.001282205   -0.005173659    -0.010428756    -0.015718374
    -0.020976354    -0.026182152    -0.031379677    -0.036592884    -0.041797588
        -0.047003341    -0.052230085    -0.05746015     -0.062684545
    -0.067910314    -0.073135697    -0.078361903    -0.083593206    -0.088853693
        -0.094091179    -0.09922596     -0.104333642    -0.109477151
    -0.114625219    -0.119760428    -0.124894764    -0.130046333    -0.135195295
        -0.140327092    -0.145446345    -0.150552923    -0.155649595
    -0.16073237     -0.165796328    -0.170855286    -0.175937421    -0.181061804
        -0.186230194    -0.191432911    -0.196659083    -0.201915382
    -0.207171197    -0.21238155     -0.217579834    -0.222791109    -0.228000876
        -0.233217891    -0.238414564    -0.243551204    -0.248662169
    -0.253765909    -0.258836899    -0.263864595    -0.268828791    -0.273697089
        -0.278476209    -0.283218992    -0.288028761    -0.292975513
    -0.298007407    -0.303083525    -0.308214338    -0.313393251    -0.318604433
        -0.323834099    -0.329071737    -0.334307818    -0.339538405
    -0.344767747    -0.348691738
];
A=flip(A_input,2);
x=flip(x_input,2);

%inputs
gamma=1.4;
patm=101325;%[Pa]
shock=true; %CHANGE THIS TO TRUE TO ENABLE SHOCK
```

```
shock_position=45; %45 is the position closest to example 5.6 of Aero III book

if shock
    limit=shock_position;
else
    limit=length(A);
end

%solves isentropic relation
count=1;
for i=1:(limit)
    if count<30
        Mt1=0.09;
    else
        Mt1=2;
    end
    Mt2=0;
    flag = true;
    while flag
        Mt2 = Mt1 - m(gamma,Mt1,A(i))/der(gamma,Mt1);
        if abs(Mt1-Mt2)<1*10^-6
            flag = false;
        else
            Mt1 = Mt2;
        end
    end
            M(i)=Mt2;
            count=count+1;

end

if shock
%Properties after and before shock: x is before shock and y after shock
    Mx = M(shock_position);
    My = sqrt((Mx^2+2/(gamma-1))/(2*gamma*Mx^2/(gamma-1)-1));
%Update critical area values after shock
    Axy_Acrit1=A(shock_position);
    Axy_Acrit2= (2*(1+(gamma-1)*0.5*My^2)/(gamma+1))^((gamma+1)/(2*gamma-2))/
       My;
    A_new=A*Axy_Acrit2/Axy_Acrit1;

    for i=(shock_position+1):(length(A))
    Mt1=0.09;
    Mt2=0;
    flag = true;
    while flag
        Mt2 = Mt1 - m(gamma,Mt1,A_new(i))/der(gamma,Mt1);
```

```
        if abs(Mt1-Mt2)<1*10^-6
            flag = false;
        else
            Mt1 = Mt2;
        end
    end
            M(i)=Mt2;
            count=count+1;
    end
end

figure(1)
hold on
plot(x,A,"k",LineWidth=3)
plot(x,M,'r.',"MarkerSize",20)
if shock
    position=(x(shock_position)+x(shock_position+1))/2;
    xl3=xline(position,'--k',{'Shockwave'});
    xl3.LabelVerticalAlignment = 'top';
    xl3.LabelHorizontalAlignment = 'left';
    xl3.FontSize = 9;
end
legend("A/Acrit1","Mach",'Location','east')
axis([-0.35 0 0 3.1])

r_T_T0=1./(1+M.^2*(gamma-1)/2);
r_p_p0=(r_T_T0).^(gamma/(gamma-1));
if shock
    r_py_px = 1+2*gamma*(Mx^2-1)/(gamma+1);
    r_p02_py =(1+(gamma-1)*My^2/2)^(gamma/(gamma-1));
    r_px_p01 =(1+(gamma-1)*Mx^2/2)^(gamma/(1-gamma));
    r_p02_p01=r_p02_py*r_py_px*r_px_p01;
    p02=patm/r_p_p0(end)
    p0=p02/r_p02_p01
    count_2 = 1;
    for i=1:(length(A))
            if shock_position>=count_2
                p(i)=r_p_p0(i)*p0; %01conditions
            elseif shock_position<count_2
                p(i)=r_p_p0(i)*p02;%02 conditions
            end

            count_2 = count_2 + 1;
    end

else
p0=patm/r_p_p0(end)
```

```
p=p0*r_p_p0;
end

figure(2)
plot(x,p)

function f = m(gama,Mt,A_ratio)
    f = (2*(1+(gama-1)*0.5*Mt^2)/(gama+1))^((gama+1)/(2*gama-2))/ Mt - A_ratio;

end

function df = der(gama,Mt)
    df = 2*(Mt^2-1)*((2+(gama-1)*Mt^2)/(gama+1))^((gama+1)/(2*gama-2))/((gama
        -1)*Mt^4+2*Mt^2);
end
```